Received: 30 April 2022 | Revised: 7 June 2022 | Accepted: 27 June 2022

DOI: 10.1111/ijac.14150

SPECIAL ISSUE ARTICLE

Hole-doped high entropy ferrites: Structure and charge compensation mechanisms in $(Gd_{0.2}La_{0.2}Nd_{0.2}Sm_{0.2}Y_{0.2})_{1-x}Ca_xFeO_3$

Luis Eiselt[1] | **Robert Kruk**[2] | **Horst Hahn**[1,2] | **Abhishek Sarkar**[1,2]

[1]KIT-TUD Joint Research Laboratory Nanomaterials, Technical University of Darmstadt, Darmstadt, Germany

[2]Institute of Nanotechnology, Karlsruhe Institute of Technology, Eggenstein-Leopoldshafen, Germany

Correspondence
Horst Hahn and Abhishek Sarkar, KIT-TUD Joint Research Laboratory Nanomaterials, Technical University of Darmstadt, Otto-Berndt-Str. 3, Darmstadt 64287, Germany.
Email: horst.hahn@kit.edu and abhishek.sarkar@kit.edu

Funding information
Deutsche Forschungsgemeinschaft, Grant/Award Number: HA 1344/43-2

Abstract

High entropy oxides (HEOs) can be defined as single-phase oxide solid solutions with five or more cations in near equiatomic proportion occupying a given cation sub-lattice. The compositional flexibility while retaining the phase purity can be considered one of the major strengths of this materials class. Taking advantage of this aspect, here we explore the extent to which an aliovalent hole dopant can be incorporated into a perovskite-HEO system. Nine systems, $(Gd_{0.2}La_{0.2}Nd_{0.2}Sm_{0.2}Y_{0.2})_{1-x}Ca_xFeO_3$, with varying amount of Ca content (x = 0–.5) are synthesized using nebulized spray pyrolysis. Single-phase orthorhombic (*Pbnm*) structure can be retained up to 20% of Ca doping. Beyond 20% of Ca, a secondary rhombohedral (*R*-3*c*) phase emerges. The ^{57}Fe Mössbauer spectra indicate that charge compensation occurs only via oxygen vacancy formation in the single-phase systems containing up to 15% of Ca. In addition, partial transition from Fe^{3+} to Fe^{4+} occurs in the 20% Ca-doped case. Room temperature Mössbauer spectroscopy further reflects the coexistence of multiple magnetic phases in crystallographic single-phase $(Gd_{0.2}La_{0.2}Nd_{0.2}Sm_{0.2}Y_{0.2})_{1-x}Ca_xFeO_3$, which is supported by magnetometry measurements. These initial results show the potential of charge doping to tune structural–magneto–electronic properties in compositionally complex HEOs, warranting further research in this direction.

KEYWORDS
magnetic materials/properties, mössbauer spectroscopy, perovskites, high entropy oxides

1 | INTRODUCTION

The search for new materials with intriguing properties has always been one of the major research interests in materials science. Research activities on an entirely new class of oxide materials, the high entropy oxide (HEO), have gained significant attention amongst the materials research community since its discovery in 2015.[1–5] HEOs are single-phase solid solutions consisting of multiple cations in near equiatomic proportions. The presence of five or more principal cations in comparable amounts results in an increased configurational entropy, as dictated

by Boltzmann's equation, hence the term "high entropy" is often used to classify these systems.[2,5] Apart from the enhanced entropy contribution, the unique multicomponent design concept offers the possibility to discover new oxide compositions close to the center of the respective phase diagrams with potentially unique properties. Keeping these motivations as the focal points, the field of HEOs has rapidly grown to include several compositions and crystallographic structures, such as rock salt, fluorite, perovskite, spinel, bixbyite, and pyrochlore.[1,6–14] Furthermore, multiple studies already highlight the improved functionalities exhibited by the HEOs, such as enhanced electrochemical cyclic stability, high catalytic activity, tailorable optical, and magnetic properties.[6,15–22]

The focus of this work is on perovskite (ABO_3)-type HEOs that consist of five different rare earth cation on the A-site sub-lattice and Fe on the B-site sub-lattice, $(Gd_{0.2}La_{0.2}Nd_{0.2}Sm_{0.2}Y_{0.2})FeO_3$. The system is chosen based on our preceding works, which showed that despite the compositional complexity $(Gd_{0.2}La_{0.2}Nd_{0.2}Sm_{0.2}Y_{0.2})FeO_3$ crystallizes in a single-phase orthorhombic perovskite structure and exhibits a high magnetic transition temperature, $T_N \approx 675$ K.[7,18] The canted antiferromagnetism in the system is accompanied by a high coercive field, $H_c \approx 2$ T, at room temperature along with spin-reorientation transition below 150 K.[18] Structural and functional properties of the conventional ferrite perovskite systems, such as $LaFeO_3$ and $SmFeO_3$, are traditionally tailored using charge doping.[23–26] In fact, the related charge compensation mechanisms via oxygen defects or oxidation/reduction of the accompanying cations especially that of Fe play a pivotal role in determining both the structure and properties of the doped ferrite perovskites. Based on this premise, it is of fundamental as well as practical interest to evaluate the structural flexibility and charge compensation mechanisms in compositionally complex perovskite-type high entropy ferrites. In this study, Ca is chosen as the hole dopant in $(Gd_{0.2}La_{0.2}Nd_{0.2}Sm_{0.2}Y_{0.2})_{1-x}Ca_xFeO_3$ because of its stable 2+ oxidation state and comparable ionic radii to that of the trivalent rare-earth (RE) cations. Utilizing X-ray diffraction (XRD), Mössbauer spectroscopy and magnetometry, the changes in the lattice parameters as well as the overall crystallographic structure and phase composition along with the nature of charge compensation mechanism are investigated in $(Gd_{0.2}La_{0.2}Nd_{0.2}Sm_{0.2}Y_{0.2})_{1-x}Ca_xFeO_3$ ($x = 0$–.5).

2 | EXPERIMENTAL PROCEDURES

The powder samples were synthesized using nebulized spray pyrolysis technique. The details of the synthesis procedure can be found elsewhere.[27] A total of nine samples were synthesized with 0%, 5%, 10%, 15%, 20%, 25%, 30%, 40% and 50% of the RE elements substituted by Ca, with the corresponding chemical formula $(Gd_{0.2}La_{0.2}Nd_{0.2}Sm_{0.2}Y_{0.2})_{1-x}Ca_xFeO_3$ where $x = 0$, .05, .1, .15, .20, .25, .30, .40, .50, respectively. Aqueous-based precursor solutions with a concentration of .1 mol/L were prepared by dissolving a stoichiometric amount of nitrate salts of the metal cations, $Gd(NO_3)_3{\cdot}6H_2O$, $La(NO_3)_3{\cdot}6H_2O$, $Nd(NO_3)_3{\cdot}6H_2O$, $Sm(NO_3)_3{\cdot}6H_2O$, $Y(NO_3)_3{\cdot}6H_2O$, $Fe(NO_3)_3{\cdot}9H_2O$, $Ca(NO_3)_2{\cdot}4H_2O$, in deionized water. The mist of the precursor solution generated from the piezo-driven nebulizer was transported to the hot-wall reactor using N_2 as the carrier gas (5 slpm). The hot-wall reactor was maintained at a temperature of 1050°C and a pressure of 900 mbar. The as-synthesized powders were collected using a filter-based collector and calcined at 1200°C for 2.5 h in air atmosphere with a heating and cooling rate of 10°C/min. These calcined samples are used for further characterizations.

Room temperature XRD patterns of the powder samples were recorded using a Bruker D8 Advance with Bragg–Brentano geometry using Cu-K_α radiation with an Ni filter and an LYNXEYE detector having a fixed divergence slit (.3°). A step size of .02° and a collection time of 4 s per step at 30 kV and 40 mA over the diffraction angle (2Θ) range between 10° and 90° were used. Rietveld analysis of the XRD patterns was performed using TOPAS V.7. (Academic version) and FullProf to determine the structure and phase composition of the powders. The instrumental intensity distribution for the XRD data was determined using a reference scan of LaB6 (NIST 660a). Thermal displacement parameters were constrained to be the same for all atoms.

^{57}Fe Mössbauer spectroscopy was performed using a ^{57}Co:Rh source in transmission geometry with a triangular sweep of the velocity scale. The spectra were fitted using the WinNormos-for-Igor software. As conventionally done, all center shifts are given relative to α-Fe at room temperature.

Magnetic measurements at room temperature were performed using a Quantum Design MPMS3 superconducting quantum interference device (SQUID) in a vibrating sample magnetometer mode.

3 | RESULTS AND DISCUSSION

3.1 | Structural analysis

Figure 1 represents the XRD pattern of all the nine samples, $(Gd_{0.2}La_{0.2}Nd_{0.2}Sm_{0.2}Y_{0.2})_{1-x}Ca_xFeO_3$. No secondary non-perovskite phases can be observed in any of the studied compositions. The undoped base system,

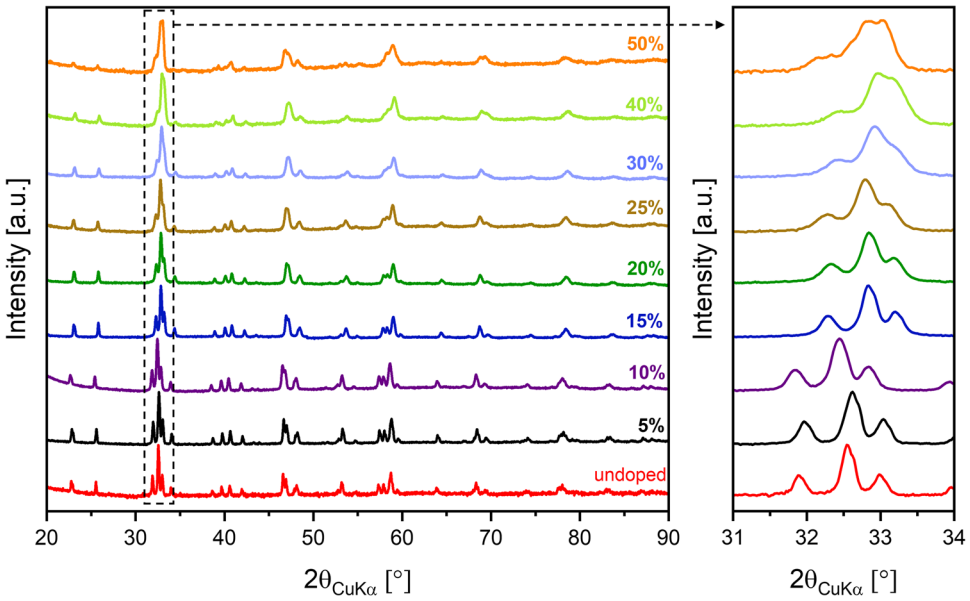

FIGURE 1 X-ray diffraction (XRD) pattern of $(Gd_{0.2}La_{0.2}Nd_{0.2}Sm_{0.2}Y_{0.2})_{1-x}Ca_xFeO_3$. In the figure, the amount of Ca doping is represented in percentage, for example, 5% means $x = .05$ in the formula. The undoped sample represents $x = 0$. The zoomed-in graph shows the structural transition upon increasing amount of Ca doping

$(Gd_{0.2}La_{0.2}Nd_{0.2}Sm_{0.2}Y_{0.2})FeO_3$ exhibits a single-phase orthorhombic structure (space group *Pbnm*), which is in agreement with the earlier reports.[7,18] However, with increasing Ca doping, pertinent changes in peak positions and relative intensities are visible. The zoomed-in portion in Figure 1 shows the (0 2 0), (1 1 2), (2 0 0) peaks of the orthorhombic phase, which indicate a gradual shift in the peak positions toward higher angles with an increasing amount of Ca doping. This primarily indicates a reduction of the lattice parameters upon Ca doping. Apart from the shift in the peak positions, a gradual change of the relative intensities of the three distinct peaks in the range of $2\theta \approx 32°–33.5°$, that is, (0 2 0), (1 1 2), (2 0 0), especially at higher Ca doping, can also be observed from the zoomed part of Figure 1. A similar change in the peak feature is also evident for the peaks at $2\theta = 46.5°–48.5°$ and $2\theta = 57.5°–59.5°$. These changes indicate a change in the crystallographic structure upon a higher amount of Ca doping.

In order to better understand the structural changes upon Ca doping, the Rietveld refinement of the XRD patterns was performed. All the systems up to a Ca doping of 20% could be fitted with a single-phase orthorhombic structure as shown in Figure 2A–D. The details of the refinement are summarized in Table S1. For systems with Ca amount 25% or higher, an additional rhombohedral phase (*R*-3*c*) perovskite phase was required to adequately fit the XRD pattern. In the system with 25% Ca content on the A-site, a slight increase in fluctuations in the residual curve could be observed when only the *Pbnm* phase was used for fitting, as shown in Figure S1a. This provides a first hint of the presence of a secondary phase. More prominent evidence of the secondary phase can be observed from the increased misfit of the (2 2 0) and (0 0 4) peaks at around 46.5°–47.5° as highlighted in Figure S1b. In order to achieve a better refinement, a minor amount (3.1 wt.%) of secondary rhombohedral phase was introduced. It should be noted that the identification of the second perovskite phase in this system is not straightforward due to several possible symmetry-related crystallographic sub/super-groups of *Pbnm*. Furthermore, for refinement using a dual phase fit, the composition of both the orthorhombic and rhombohedral phases are considered identical, as a distinction between the constituent RE elements is not possible from XRD. A similar transition from an orthorhombic to rhombohedral perovskite phase is also observed in conventional hole-doped ferrites, such as $La_{1-x}Sr_xFeO_3$ with Sr amount more than 20%.[23] The result of the dual phase (*Pbnm* + *R*-3*c*) fit is shown in Figure S2a. To show the improvement in quality of the refinement upon using two phases, the critical region around 47° is shown Figure S2b. For the 30% Ca-doped system, the difference between experimental and calculated pattern continues to increase when using a single orthorhombic phase for fitting, Figure 3A. The change in the XRD patterns for the peaks around 47° also progresses, with both peaks approaching similar intensity, in contrast to the lower dopant compositions where the lower angle peak was more intense. In addition, the (2 0 0) orthorhombic peak next to the highest intensity (1 1 2) orthorhombic peak at $2\theta = 32.78°$ keeps moving closer to the latter, while simultaneously gaining in

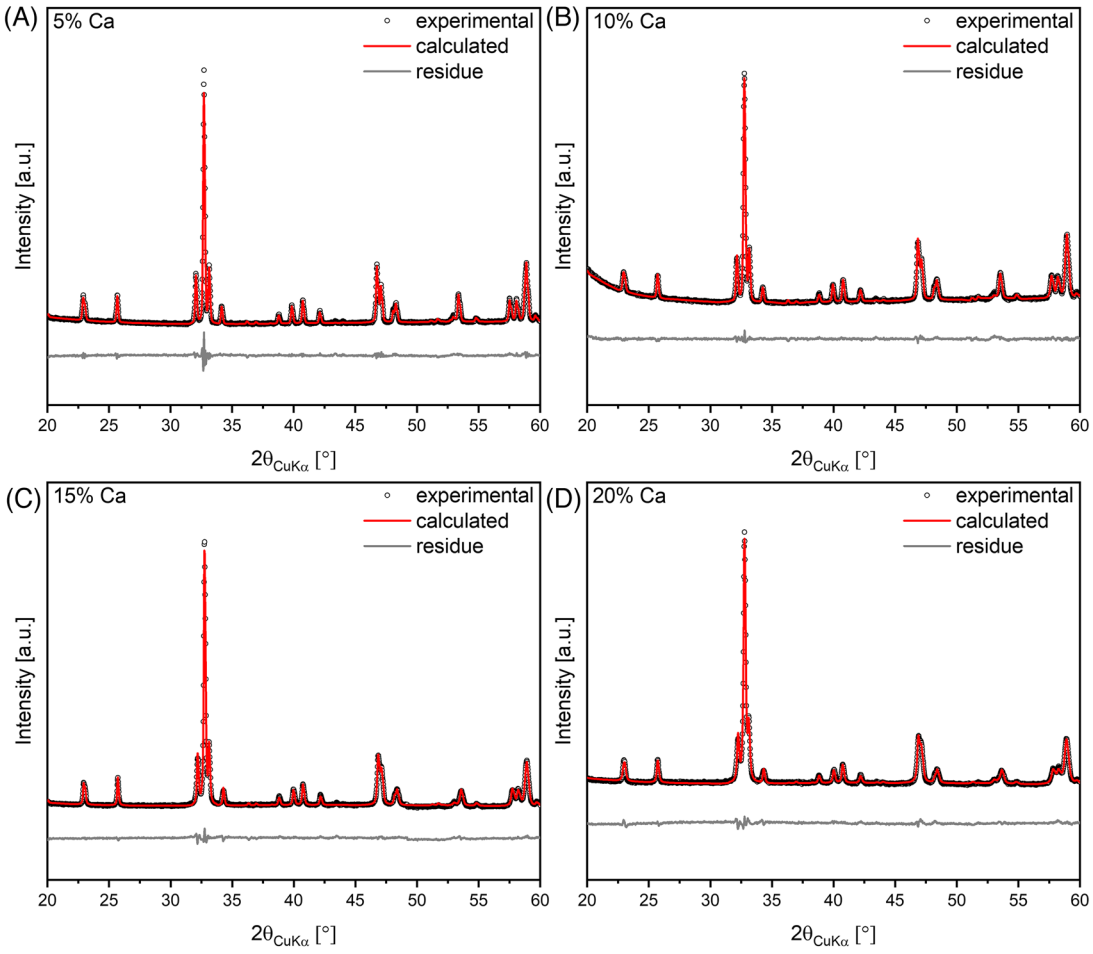

FIGURE 2 Rietveld refinement confirming the single-phase orthorhombic structure of $(Gd_{0.2}La_{0.2}Nd_{0.2}Sm_{0.2}Y_{0.2})_{1-x}Ca_xFeO_3$ with $x = .05$ (A), .10 (B), .15 (C) and .20 (D)

intensity. Both zoomed regions in Figure 3A cannot be well described using a single orthorhombic phase fit. Therefore, an additional secondary rhombohedral phase is once again used to achieve a better fit. The result of the dual phase fit is depicted in Figure 3B. Nevertheless, the amount of the secondary rhombohedral phase is still rather minor, 8.6 wt.%. The difference between the experimental and calculated spectra increases considerably for the 40% Ca-doped sample when only a single orthorhombic phase is used for fitting, see Figure S3a. The dual-phase refinement, presented in Figure S3b, shows a relative improvement in the quality of the fit; however, it no longer reaches the quality of the fitting obtained for the samples with lower doping percentage. This is most apparent when the fit is compared around zoomed-in regions, as shown in Figure S3b. The amount of secondary rhombohedral phase is calculated to be around 31.1 wt.% for the 40% Ca-doped system. The XRD pattern of the 50% Ca sample composition posed the greatest challenge. The pattern could not be reasonably described either using a single orthorhombic or a single rhombohedral phase fit. The dual-phase fit appears to yield a reasonable result as is shown in Figure S4a. However, looking at the zoomed-in region of Figure S4b a deviation of experimental pattern from the fitted one can be clearly observed. This reflects that the dual-phase approach with *Pbnm* and *R*-3*c* might not be adequate for this particular sample, 50% Ca. The misfit between experimental and calculated patterns plausibly points toward the emergence of a third phase. More detailed local structural investigation will be required to fully understand the phase composition of this system. Nevertheless, in contrast to the systems with lower Ca doping, the sample with 50% doping shows a major rhombohedral phase, the amount calculated from the dual phase fit is 89.9%.

The average lattice parameters for the main orthorhombic phase that have been obtained from the Rietveld refinement are presented in Figure 4A. Although the a and $c/\sqrt{2}$ remain largely constant, a gradual decrease in the b with increase of the Ca doping can be observed throughout the entire single-phase region. The observed changes in the lattice parameters further support the

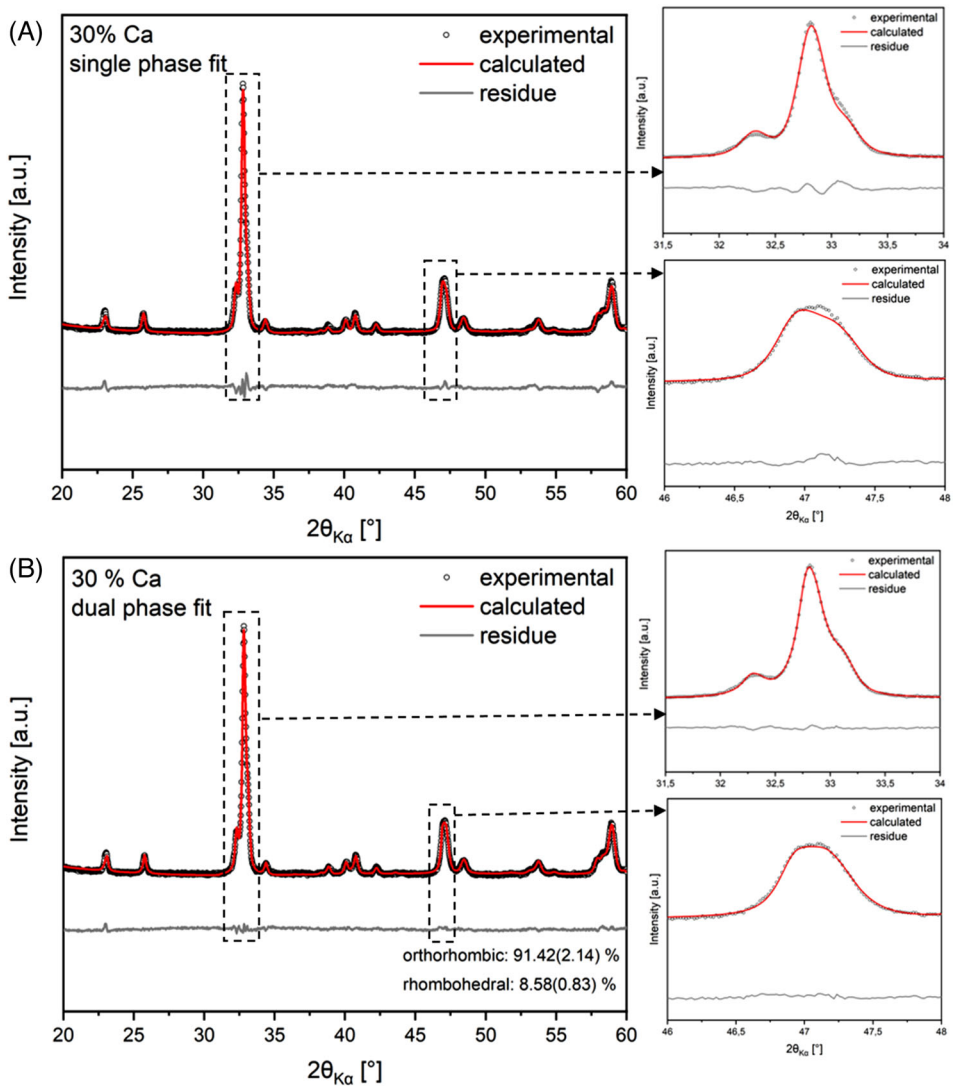

FIGURE 3 (A) Single-phase orthorhombic (*Pbnm*) and (B) dual-phase orthorhombic + rhombohedral (*Pbnm* + *R*-3*c*) refined patterns of 30% Ca-doped $(Gd_{0.2}La_{0.2}Nd_{0.2}Sm_{0.2}Y_{0.2})_{1-x}Ca_xFeO_3$

gradual transition from orthorhombic to rhombohedral phase. In order to quantify the evolution of distortion in the main orthorhombic phase, metric distortion, ε, (Equation 1) and Goldschmidt's tolerance factor, t, (Equation 5) are compared in Figure 4B:

$$\varepsilon = \left(\frac{1}{3}\right) \cdot \left[\left\{ \frac{a_{norm} - a_{ps.cubic}}{a_{ps.cubic}} \right\}^2 + \left\{ \frac{b_{norm} - a_{ps.cubic}}{a_{ps.cubic}} \right\}^2 + \left\{ \frac{c_{norm} - a_{ps.cubic}}{a_{ps.cubic}} \right\}^2 \right]^{0.5} \quad (1)$$

where $a_{ps.cubic}$ is the pseudo-cubic lattice parameter, a_{norm}, b_{norm}, c_{norm} are the normalized values of pseudo-cubic lattice parameters taking into account the orientation of the lower symmetry cell. These values are calculated from the following equations:

$$a_{ps.cubic} = \sqrt[3]{V} \quad (2)$$

$$a_{norm} = \frac{a}{\sqrt{2}\sqrt[3]{V}}, \quad b_{norm} = \frac{b}{\sqrt{2}\sqrt[3]{V}}, \quad c_{norm} = \frac{c}{2\sqrt[3]{V}} \quad (3)$$

where V is the volume per ABO_3 unit, that is,

$$V = \frac{a \times b \times c}{4} \quad (4)$$

with *a, b, c* being the original lattice parameter of the orthorhombic (*Pbnm*) perovskites obtained from the Rietveld analysis (Table S1). The t is calculated using the

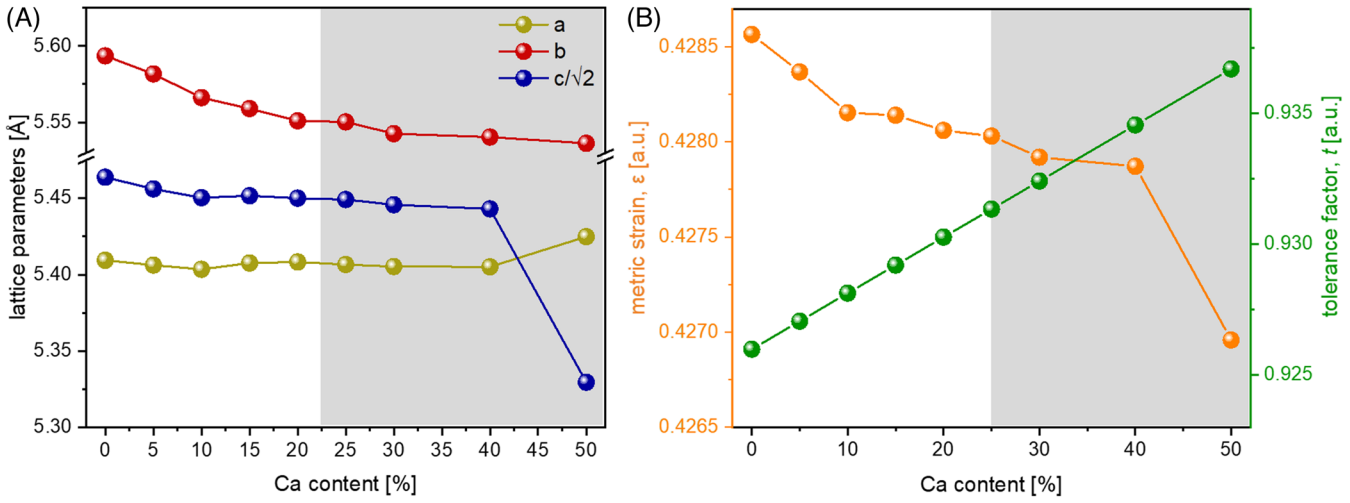

FIGURE 4 (A) Progression of the lattice parameters obtained from the Rietveld refinement and (B) comparison between tolerance factor (t) and metric strain (ε) of $(Gd_{0.2}La_{0.2}Nd_{0.2}Sm_{0.2}Y_{0.2})_{1-x}Ca_xFeO_3$. The gray area indicates the compositional range where a secondary perovskite phase is observed

following equation:

$$t = \frac{r_A + r_O}{\sqrt{2}(r_B + r_O)} \quad (5)$$

where r_A and r_B are the ionic radii[28] of the cation at A- and B-site, respectively, and r_o is the radius of the oxygen ion. In the case of A-site, the average of the ionic radii is considered.

The value of ε is the experimental yardstick highlighting the amount of deviation from the ideal cubic perovskite structure. The ε is a crucial parameter in orthorhombic (ABO_3) perovskites as it is directly correlated to the tilting of the BO_6 octahedra, which strongly influences the exchange interactions governing the magnetic properties in perovskites. Figure 4B indicates that the t linearly increases upon Ca doping but stays below the threshold for cubic structures ($t \approx 1$). The gradual increase in t with increasing Ca content implies a decrease in structural distortion. This is further substantiated by the degree of ε being lowered with increasing amount of Ca doping. The dependency of t and ε as a function of Ca doping is intuitive, as on one hand the mean A-site radius slightly increases due to substitution of the rare-earth cations by slightly larger Ca^{2+} and on the other hand the mean ionic radius of the B-site Fe-cation can potentially decrease due to possible conversion of Fe^{3+} (.645 Å) to Fe^{4+} (.585 Å).[28]

Overall, from the structural investigation, it can be concluded that $(Gd_{0.2}La_{0.2}Nd_{0.2}Sm_{0.2}Y_{0.2})FeO_3$ can accommodate up to 20% Ca doping while retaining a single orthorhombic phase. Further increase of the doping level results in a gradual transition of the orthorhombic phase to rhombohedral phase; however, neither a single orthorhombic nor rhombohedral phase prevails beyond 20% Ca. The structural results obtained here can be intimately related to the charge compensation mechanism due to the aliovalent Ca doping. The charge compensation mechanism in $(Gd_{0.2}La_{0.2}Nd_{0.2}Sm_{0.2}Y_{0.2})_{1-x}Ca_xFeO_3$ should either occur via formation of oxygen vacancies or transformation of Fe^{3+} to Fe^{4+} or both, as change in the oxidation state of the RE^{3+} cations is not feasible. Given the strength of ^{57}Fe Mössbauer spectroscopy to unravel the oxidation, coordination, magnetic and spin-electronic state of Fe, it is used to further study the charge compensation mechanism in $(Gd_{0.2}La_{0.2}Nd_{0.2}Sm_{0.2}Y_{0.2})_{1-x}Ca_xFeO_3$.

3.2 | ^{57}Fe Mössbauer spectroscopy

The room temperature Mössbauer spectra for all single-phase samples, that is, up to 20% Ca doping are presented in Figure 5. Measurements for the other samples with more Ca are not presented as XRD confirmed the formation of a secondary phase at 25% Ca and beyond. All the spectra in Figure 5 represent distinct hyperfine splitting (sextet), implying magnetic ordering at room temperature and transition temperature above it. A lowering of the magnetic hyperfine filed (B_{hf}) denoted by the shrinking of the magnetic sextet splitting is apparent upon increasing the Ca amount. In addition, it can be observed (Figure 5) that with the increasing Ca-doping intensity ratios of the outer peaks (indicated by lines 1, 6 in Figure 5) to that of the inner peaks (indicated by lines 2, 3, 4 and 5 in Figure 5) deviate from the ideal value of a

TABLE 1 Hyperfine parameters obtained from fitting of the ^{57}Fe Mössbauer spectra of single-phase $(Gd_{0.2}La_{0.2}Nd_{0.2}Sm_{0.2}Y_{0.2})_{1-x}Ca_xFeO_3$ ($x = 0, .05, .10, .15$ and $.20$) measured at 300 K, B_{hf} is the hyperfine field, δ_{iso} is the isomer shift and QS is the quadrupole line shift

Ca amount (%)	Fe environment	B_{hf} (T)	QS (mm/s)	δ_{iso} (mm/s)	Area (%)
0	Sextet	50.98(1)	.002	.368(4)	100
5	Sextet 1	50.18(1)	.004(3)	.369(2)	83
	Sextet 2	47.82(5)	.01(2)	.360(6)	17
10	Sextet 1	49.49(3)	.007(6)	.368(3)	72.7
	Sextet 2	46.72(6)	.01(2)	.373(7)	27.3
15	Sextet 1	48.60(4)	.006(6)	.371(4)	73.9
	Sextet 2	44.41(8)	.01(2)	.360(7)	26.1
20	Sextet 1	48.27(2)	.026(3)	.361(2)	67.8
	Sextet 2	42.77(4)	.003(9)	.321(5)	21.5
	Singlet			.112(8)	10.7

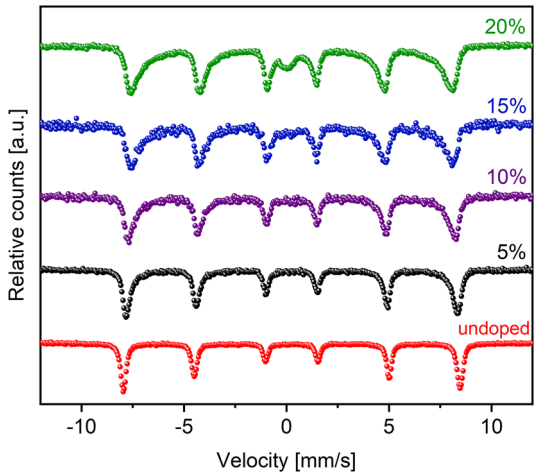

FIGURE 5 Room temperature Mössbauer spectra indicating magnetic ordering in the single-phase $(Gd_{0.2}La_{0.2}Nd_{0.2}Sm_{0.2}Y_{0.2})_{1-x}Ca_xFeO_3$ samples. The asymmetry in the peak shape increases with increasing Ca doping. A decrease in the intensity of the outermost lines (1, 6) compared to that of the inner lines (2, 3, 4 and 5) can be observed as the amount of Ca doping increases

static single sextet spectrum, which should be 3:2:1:1:2:3 for the lines 1–6. This observed lowering of the relative intensity ratio of the outer to the inner lines can indicate either dynamic character of the spectra (spin fluctuation close to transition temperature) or the presence of multiple Fe magnetic environments. The latter scenario is more likely as, in contrast to the undoped system, strong peak asymmetry can be observed in all the Ca-doped systems. Hence, the interpretation of results based on a single sextet model is not adequate to explain the Mössbauer spectra of the Ca-doped systems. Thus, to gain better insights into the complex local magnetic properties of Fe fitting of the Mössbauer spectra with a distribution of hyperfine (B_{hf}) parameters is necessary. The results obtained from the fitted data are presented in Figures 6A, S5, S6, and Table 1.

A gradual lowering of the average B_{hf} is observed with increasing Ca doping, as shown in Figure 6B. In addition to the magnetic sextet distribution a singlet is present in the 20% Ca system, Figure 6C. In the case of the Ca-doped systems, a shoulder at the lower B_{hf} can be observed. Based on this observation a dual sextet fit is attempted, one with a higher B_{hf} and the other with a lower B_{hf}. The dual-sextet-based fitting provides reasonable results as shown in Figure S6 with the hyperfine parameters summarized in Table 1. The results indicate that there are two major Fe environments in the Ca-doped systems with close isomer shifts (δ_{iso}). This can be an indication of the magneto-electronic phase separation in crystallographic single-phase structure, which is a typical characteristic of HEOs.[4,17] Furthermore, the presence of more than one Fe magnetic environment reflects a variation in the Fe–O–Fe bonds in the Ca-doped single-phase systems, which possibly originates from presence of oxygen vacancies that can significantly alter the Fe–O–Fe bonding characteristics. Based on the δ_{iso} of both the magnetic sextets (Table 1 and Figure S6) and the average δ_{iso} obtained from the distribution fit (Figure S5), it can be safely concluded that Fe is present in solely 3+ oxidation state in 5%, 10% and 15% Ca-doped systems, as is the case for the undoped system. Hence, in these systems, the charge compensation occurs fully via oxygen vacancies formation. The result is not surprising as HEOs are known for accommodating large fractions of oxygen vacancies.[6,29,30] In the case of 20% Ca-doped system, the singlet with $\delta_{iso} = .11$ mm/s relative to α-Fe corresponds to Fe^{4+}. However, the amount of Fe^{4+} is close to 10.7%, which indicates that even in this system the remaining 9.3% of Ca dopant is accommodated via oxygen vacancies formation. Furthermore, the 20% Ca-doped system presents a unique three-phase environment of Fe at room temperature, the two sextets corresponding

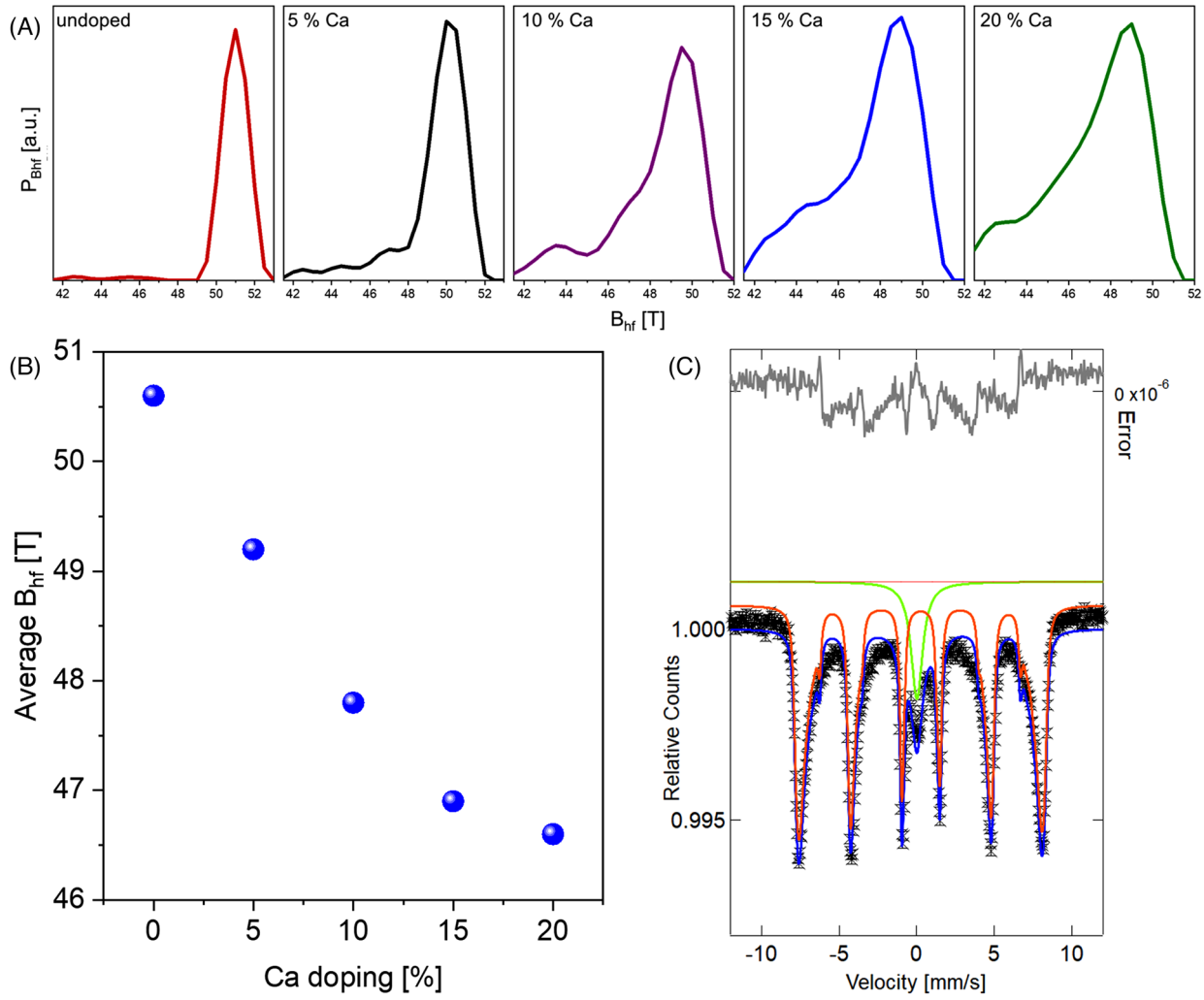

FIGURE 6 (A) Hyperfine distribution of room temperature Mössbauer spectra of the single-phase $(Gd_{0.2}La_{0.2}Nd_{0.2}Sm_{0.2}Y_{0.2})_{1-x}Ca_xFeO_3$ samples. (B) The average hyperfine field obtained from the distribution fit as a function of the Ca doping. (C) Fitted spectrum (blue curve) of 20% Ca, where a singlet (green curve) is required in addition to the hyperfine distribution (red curve) to adequately fit the experimental data (black cross)

to magnetically ordered Fe^{3+} and the singlet corresponding to non-magnetic Fe^{4+}. Interestingly, despite the coexistence of three different magnetic environment of Fe, the 20% Ca-doped system is still crystallographically phase-pure.

3.3 | Room temperature magnetic hysteresis (M–H) measurements

The M–H curves presented in Figure 7 are largely linear with no sign of saturation even at the highest field of 5 T. These results, which are similar the observation for the undoped $(Gd_{0.2}La_{0.2}Nd_{0.2}Sm_{0.2}Y_{0.2})FeO_3$,[17] indicate that predominant (canted) antiferromagnetic ordering prevails even in the Ca-doped system. Similar to $(Gd_{0.2}La_{0.2}Nd_{0.2}Sm_{0.2}Y_{0.2})FeO_3$, large H_c are observed in the Ca-doped systems, which stem from the magnetocrystalline anisotropy of the canted antiferromagnetic spins. In contrast to the $(Gd_{0.2}La_{0.2}Nd_{0.2}Sm_{0.2}Y_{0.2})FeO_3$, kinks in the M–H curves can be observed for all the Ca-doped system, which is most prominent for the 15% Ca-doped system. The kinks in the M–H curve indicate magnetic phase separation that most likely originates from a secondary soft magnetic phase $(Gd_{0.2}La_{0.2}Nd_{0.2}Sm_{0.2}Y_{0.2})_{1-x}Ca_xFeO_3$. The result is in good agreement with the two separate magnetic sextets observed in the Mössbauer spectra of $(Gd_{0.2}La_{0.2}Nd_{0.2}Sm_{0.2}Y_{0.2})_{1-x}Ca_xFeO_3$, where the sextet with lower B_{hf} plausibly corresponds to the soft magnetic phase, whose relative fraction is the highest (26.1%) for the 15% Ca-doped system. Nevertheless, dedicated temperature-dependent Mössbauer spectroscopy and magnetometery are required in future to unravel the

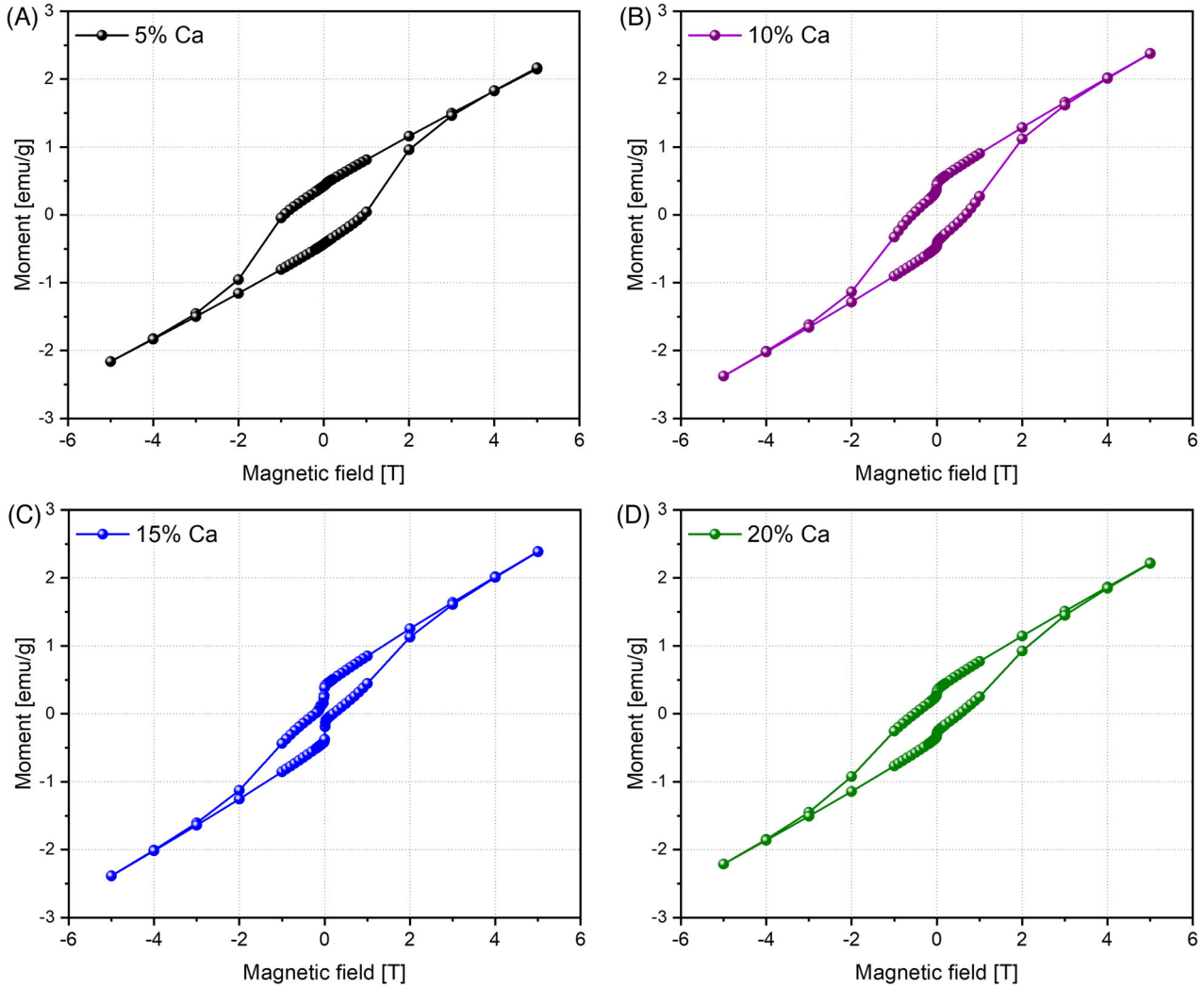

FIGURE 7 Room temperature magnetization measurements with clear indications of magnetic hysteresis for $(Gd_{0.2}La_{0.2}Nd_{0.2}Sm_{0.2}Y_{0.2})_{1-x}Ca_xFeO_3$, (A) x = .05, (B) x = .10, (C) x = .15 and (D) x = .20. The kinks in the hysteresis plot, more prominent in 15% Ca-doped system, indicate the possible presence of secondary soft magnetic phase in addition to the dominant canted antiferromagnetic phase

exotic magnetic properties of charge-doped high entropy ferrites.

4 | CONCLUSIONS

In this study, the effect of hole (Ca^{2+}) doping in a perovskite-type high entropy ferrite system, $(Gd_{0.2}La_{0.2}Nd_{0.2}Sm_{0.2}Y_{0.2})FeO_3$ was explored. Amongst the nine systems studied, $(Gd_{0.2}La_{0.2}Nd_{0.2}Sm_{0.2}Y_{0.2})_{1-x}Ca_xFeO_3$ (x = 0, .05, .10, .15, .20, .25, .30, .40, .5), five (x = 0, .05, .10, .15, .20) crystallized in a single-phase orthorhombic structure. Noticeable decrease in metric distortion of the orthorhombic phase is observed with increasing Ca doping. Higher Ca-doped systems (x = .25, .30, .40, .5) exhibited two crystallographic phases, orthorhombic (*Pbnm*) and rhombohedral (*R*-3c), with an increasing amount of rhombohedral phase upon higher Ca doping. The charge compensation mechanism in the 5%, 10% and 15% Ca-doped system occurs via oxygen vacancy formation as no change in the oxidation state of Fe^{3+} is observed. In the case of 20% Ca-doped system, the charge compensation occurs partly via oxygen vacancy formation and partly by transition of Fe^{3+} to Fe^{4+}. Distinct hyperfine splitting of the Mössbauer spectra of the single-phase systems (x = 0, .05, .10, .15, .20) confirms magnetic ordering at room temperature. In contrast to the undoped system, Mössbauer spectroscopy highlighted the presence of multiple magnetic phases in the Ca-doped $(Gd_{0.2}La_{0.2}Nd_{0.2}Sm_{0.2}Y_{0.2})_{1-x}Ca_xFeO_3$ (x = 0, .05, .10, .15, .20). This result was further complemented by magnetometry measurements. Encapsulation of multiple magnetic

phases in a crystallographic single-phase structure is a behavior unique to HEOs, which in the case of high entropy ferrite is enhanced by the charge doping. Although this primary investigation sheds light on the complex magnetic behavior of $(Gd_{0.2}La_{0.2}Nd_{0.2}Sm_{0.2}Y_{0.2})_{1-x}Ca_xFeO_3$, future studies are necessary to understand the evolution of magnetism on the local scale in hole-doped high entropy ferrites.

ACKNOWLEDGMENT

H.H. and A.S. acknowledge the financial support from the Deutsche Forschungsgemeinschaft (DFG) project HA 1344/43-2.

Open access funding enabled and organized by Projekt DEAL.

ORCID

Horst Hahn https://orcid.org/0000-0001-9901-3861
Abhishek Sarkar https://orcid.org/0000-0001-9444-8241

REFERENCES

1. Rost CM, Sachet E, Borman T, Moballegh A, Dickey EC, Hou D, et al. Entropy-stabilized oxides. Nat Commun. 2015;6(1):8485. https://doi.org/10.1038/ncomms9485
2. Sarkar A, Breitung B, Hahn H. High entropy oxides: the role of entropy, enthalpy and synergy. Scr Mater. 2020;187:43–8. https://doi.org/10.1016/j.scriptamat.2020.05.019
3. Musicó BL, Gilbert D, Ward TZ, Page K, George E, Yan J, et al. The emergent field of high entropy oxides: design, prospects, challenges, and opportunities for tailoring material properties. APL Mater. 2020;8(4):040912. https://doi.org/10.1063/5.0003149
4. Sarkar A, Kruk R, Hahn H. Magnetic properties of high entropy oxides. Dalton Trans. 2021;50(6):1973–82. https://doi.org/10.1039/D0DT04154H
5. Sarkar A, Wang Q, Schiele A, Chellali MR, Bhattacharya SS, Wang D, et al. High-entropy oxides: fundamental aspects and electrochemical properties. Adv Mater. 2019;31(26):1806236. https://doi.org/10.1002/adma.201806236
6. Sarkar A, Eggert B, Velasco L, Mu X, Lill J, Ollefs K, et al. Role of intermediate 4 f states in tuning the band structure of high entropy oxides. APL Mater. 2020;8(5):051111. https://doi.org/10.1063/5.0007944
7. Sarkar A, Djenadic R, Wang D, Hein C, Kautenburger R, Clemens O, et al. Rare earth and transition metal based entropy stabilised perovskite type oxides. J Eur Ceram Soc. 2018;38(5):2318–27. https://doi.org/10.1016/j.jeurceramsoc.2017.12.058
8. Dąbrowa J, Stygar M, Mikuła A, Knapik A, Mroczka K, Tejchman W, et al. Synthesis and microstructure of the (Co,Cr,Fe,Mn,Ni)3O4 high entropy oxide characterized by spinel structure. Mater Lett. 2018;216:32–6. https://doi.org/10.1016/j.matlet.2017.12.148
9. Sarkar A, Eggert B, Witte R, Lill J, Velasco L, Wang Q, et al. Comprehensive investigation of crystallographic, spin-electronic and magnetic structure of (Co0. 2Cr0. 2Fe0. 2Mn0. 2Ni0. 2)3O4 : unraveling the suppression of configuration entropy in high entropy oxides. Acta Mater. 2022;226:117581. https://doi.org/10.1016/j.actamat.2021.117581
10. Wang J, Cui Y, Wang Q, Wang K, Huang X, Stenzel D, et al. Lithium containing layered high entropy oxide structures. Sci Rep. 2020;10(1):18430. https://doi.org/10.1038/s41598-020-75134-1
11. Kumar A, Sharma G, Aftab A, Ahmad MI. Flash assisted synthesis and densification of five component high entropy oxide (Mg, Co, Cu, Ni, Zn)O at 350°C in 3 min. J Eur Ceram Soc. 2020;40(8):3358–62. https://doi.org/10.1016/j.jeurceramsoc.2020.02.036
12. Spiridigliozzi L, Ferone C, Cioffi R, Dell'Agli G. A simple and effective predictor to design novel fluorite-structured high entropy oxides (HEOs). Acta Mater. 2021;202:181–9. https://doi.org/10.1016/j.actamat.2020.10.061
13. Usharani NJ, Shringi R, Sanghavi H, Subramanian S, Bhattacharya SS. Role of size, alio-/multi-valency and non-stoichiometry in the synthesis of phase-pure high entropy oxide (Co,Cu,Mg,Na,Ni,Zn)O. Dalton Trans. 2020;49(21):7123–32. https://doi.org/10.1039/D0DT00958J
14. Dąbrowa J, Cieślak J, Zajusz M, Mozdzierz M, Berent K, Mikuła A, et al. Structure and transport properties of the novel (Dy,Er,Gd,Ho,Y)3Fe5O12 and (Dy,Gd,Ho,Sm,Y)3Fe5O12 high entropy garnets. J Eur Ceram Soc. 2021;41:3844–9. https://doi.org/10.1016/j.jeurceramsoc.2020.12.052
15. Sarkar A, Velasco L, Wang D, Wang Q, Talasila G, de Biasi L, et al. High entropy oxides for reversible energy storage. Nat Commun. 2018;9(1):3400. https://doi.org/10.1038/s41467-018-05774-5
16. Xu H, Zhang Z, Liu J, Do-Thanh CL, Chen H, Xu S, et al. Entropy-stabilized single-atom Pd catalysts via high-entropy fluorite oxide supports. Nat Commun. 2020;11:3908. https://doi.org/10.1038/s41467-020-17738-9
17. Witte R, Sarkar A, Kruk R, Eggert B, Brand RA, Wende H, et al. High-entropy oxides: an emerging prospect for magnetic rare-earth transition metal perovskites. Phys Rev Mater. 2019;3(3):034406. https://doi.org/10.1103/PhysRevMaterials.3.034406
18. Witte R, Sarkar A, Velasco L, Kruk R, Brand RA, Eggert B, et al. Magnetic properties of rare-earth and transition metal based perovskite type high entropy oxides. J Appl Phys. 2020;127(18):185109. https://doi.org/10.1063/5.0004125
19. Karati A, Parida T, Gupta J, Adigilli HK, Borse PH, Joardar J. Band-gap engineering in novel delafossite-type multicomponent oxides for photocatalytic degradation of methylene blue. Mater Res Bull. 2021;137:111181. https://doi.org/10.1016/j.materresbull.2020.111181
20. Musicó B, Wright Q, Ward TZ, Grutter A, Arenholz E, Gilbert D, et al. Tunable magnetic ordering through cation selection in entropic spinel oxides. Phys Rev Mater. 2019;3(10):104416. https://doi.org/10.1103/PhysRevMaterials.3.104416
21. Yin Y, Shi F, Liu GQ, Tan X, Jiang J, Tiwari A, et al. Spin-glass behavior and magnetocaloric properties of high-entropy perovskite oxides. Appl Phys Lett. 2022;120(8):082404. https://doi.org/10.1063/5.0081688
22. Sarkar A, Mannava PK, Velasco L, Das C, Breitung B, Bhattacharya SS, et al. Determining role of individual cations in high entropy oxides: structure and reversible tuning of optical

properties. Scr Mater. 2022;207:114273. https://doi.org/10.1016/j.scriptamat.2021.114273

23. Clemens O, Kuhn M, Haberkorn R. Synthesis and characterization of the La1−xSrxFeO3−δ system and the fluorinated phases La1−xSrxFeO3−xFx. J Solid State Chem. 2011;184(11):2870–6. https://doi.org/10.1016/j.jssc.2011.08.037
24. Hu S, Zhang L, Liu H, Cao Z, Yu W, Zhu X, et al. Alkaline-earth elements (Ca, Sr and Ba) doped LaFeO3-δ cathodes for CO2 electroreduction. J Power Sources. 2019;443:227268. https://doi.org/10.1016/j.jpowsour.2019.227268
25. Bidrawn F, Lee S, Vohs JM, Gorte RJ. The effect of Ca, Sr, and Ba doping on the ionic conductivity and cathode performance of $LaFeO_3$. J Electrochem Soc. 2008;155(7):B660. https://doi.org/10.1149/1.2907431
26. Yo CH, Jung IY, Ryu KH, Ryu KS, Choy JH. A study of the nonstoichiometry and physical properties of the perovskite Nd1-xCaxfeo3-y system. J Solid State Chem. 1995;114:265–70. https://doi.org/10.1006/jssc.1995.1038
27. Sarkar A, Djenadic R, Usharani NJ, Sanghvi KP, Chakravadhanula VSK, Gandhi AS, et al. Nanocrystalline multicomponent entropy stabilised transition metal oxides. J Eur Ceram Soc. 2017;37(2):747–54. https://doi.org/10.1016/j.jeurceramsoc.2016.09.018
28. Shannon RD. Revised effective ionic radii and systematic studies of interatomic distances in halides and chalcogenides. Acta Crystallogr Sect A. 1976;32(5):751–67. https://doi.org/10.1107/S0567739476001551
29. Sarkar A, Loho C, Velasco L, Thomas T, Bhattacharya SS, Hahn H, et al. Multicomponent equiatomic rare earth oxides with a narrow band gap and associated praseodymium multivalency. Dalton Trans. 2017;46(36):12167–76. https://doi.org/10.1039/C7DT02077E
30. Djenadic R, Sarkar A, Clemens O, Loho C, Botros M, Chakravadhanula VSK, et al. Multicomponent equiatomic rare earth oxides. Mater Res Lett. 2017;5(2):102–9. https://doi.org/10.1080/21663831.2016.1220433

SUPPORTING INFORMATION

Additional supporting information can be found online in the Supporting Information section at the end of this article.

How to cite this article: Eiselt L, Kruk R, Hahn H, Sarkar A. Hole-doped high entropy ferrites: Structure and charge compensation mechanisms in $(Gd_{0.2}La_{0.2}Nd_{0.2}Sm_{0.2}Y_{0.2})_{1-x}Ca_xFeO_3$. Int J Appl Ceram Technol. 2023;20:213–223. https://doi.org/10.1111/ijac.14150